Reaction mechanism in the ^{20}Ne+^{59}Co system at 3–7 MeV/nucleon, and observation of entrance-channel mass-asymmetry of the incomplete fusion fraction

D. Singh,[1,2,*] R. Ali,[2] M. Afzal Ansari,[2,†] B. S. Tomar,[3] M. H. Rashid,[4] R. Guin,[4] and S. K. Das[4]

[1]*Nuclear Physics Division, Inter University Accelerator Centre, New Delhi-110067, India*

[2]*Nuclear Physics Laboratory, Department of Physics, Aligarh Muslim University, Aligarh-202002, India*

[3]*Radio-chemistry Division, Bhabha Atomic Research Centre, Trombay, Mumbai-400085, India*

[4]*Variable Energy Cyclotron Centre, 1/AF, Bidhan Nagar, Kolkata-700064, India*

(Received 27 August 2009; revised manuscript received 8 January 2011; published 9 May 2011)

Incomplete fusion of ^{20}Ne with ^{59}Co has been investigated at 3–7 MeV/nucleon using the measurement and analysis of excitation functions. The recoil-catcher technique followed by offline gamma-ray spectroscopy has been employed. Evaporation residues are found to have contributions from precursor decays, which have been separated out from the measured cumulative cross sections of evaporation residues. Measured independent cross sections are compared with PACE-2 predictions. The PACE-2 calculations are carried out for evaporation residues formed in complete fusion (CF), and the parameters are optimized so as to reproduce the cross section of evaporation residues produced exclusively in CF, e.g., *xn* and *pxn* products. With these parameters, the predicted CF cross sections for alpha emission products are calculated. Any substantial enhancement in the experimental cross section over the PACE-2 prediction is taken as a signature of incomplete fusion (ICF). The analysis indicates the occurrence of incomplete fusion involving the breakup of ^{20}Ne into ^{16}O + ^{4}He and/or ^{12}C + ^{8}Be(2α) followed by fusion of one of the fragments with the target nucleus ^{59}Co. These data also suggest that the probability of incomplete fusion increases with the projectile energy. Moreover, the ICF probability is found to increase with entrance-channel mass-asymmetry of the projectile-target systems.

DOI: 10.1103/PhysRevC.83.054604 PACS number(s): 25.70.Gh, 25.70.Jj, 25.70.Mn

I. INTRODUCTION

The study of reaction dynamics in low-energy heavy-ion-induced reactions has been the subject of resurgent interest in recent years. It has been observed that at low Z projectile ($Z \leqslant 10$), e.g. ^{12}C, ^{16}O, and ^{20}Ne when interacting with the medium and heavy mass target at projectile energy slightly above the Coulomb barrier, both the complete fusion (CF) and incomplete fusion (ICF) processes may be considered as dominant reaction mechanisms below 10 MeV/nucleon projectile energy [1]. In the case of the CF reaction, the projectile completely fuses with the target nucleus and the highly excited nuclear system decays by evaporating low-energy nucleons and the alpha particle at equilibrium stage. In the case of the ICF reaction, the projectile is assumed to break up in the nuclear field into the fragments (e.g. ^{20}Ne may break up into ^{16}O and the α particle and/or ^{12}C and ^{8}Be fragments), and one of the fragments fuses with the target nucleus and the remaining part moves in the forward direction with almost the same velocity as that of the projectile with incomplete linear momentum transfer [2]. Enough experimental data using ^{12}C and ^{16}O beams are available to believe that the ICF reaction process takes place above the Coulomb barrier [3,4]; however, information available with the ^{20}Ne beam is scarce.

Britt and Quinton [5] and Galin *et al.* [6] pointed out the breakup of projectiles ^{12}C, ^{16}O, and ^{14}N into α clusters in an interaction with the surface of target nuclei below 10 MeV/nucleon. A consistent appreciation of this process, now referred to as incomplete fusion, really emerged with the work of Inamura *et al.* [7] using the particle-gamma coincidence technique wherein they observed that the spin distribution of the residues populated through the ICF process is found to be distinctly different from those produced through the CF process. For heavy targets ($A > 120$), the only important de-excitation mode is expected to be neutron evaporation, and each product is formed essentially through a single route. In the medium mass projectile-target system, charged-particle evaporation competes with neutron evaporation in the de-excitation process, so that a given product may be formed via various different fusion modes and/or evaporation sequences, and hence, data interpretation is more complex. Earlier studies by Morgenstern *et al.* [8] carried out experiments on various projectile-target combinations, and have brought out the entrance-channel mass-asymmetry dependence of the ICF reaction, with the ICF probability being higher in a mass-asymmetric system than in a mass-symmetric system at the same relative velocity. Later on, studies by Vineyard *et al.* [9] and Chakrabarty *et al.* [10] also supported the findings of Morgenstern *et al.* [8]. However, their studies are limited to a few projectile-target combinations. Systematic measurements are, however, still required.

Various dynamical models have been proposed to explain the mechanism of ICF reactions, such as sum rule [11], breakup fusion (BUF) [12], promptly emitted particle (PEP) [13], and hot-spot model [14], etc. In the sum rule model, Wilczynski *et al.* [11] suggested that various ICF channels are localized in successive "ℓ windows" above the critical angular momentum ($\ell_{\rm crit}$) for the CF of the projectile with target. This model was somehow successful at beam energies above 10 MeV/nucleon, but failed below 8 MeV/nucleon. The BUF

*dsinghress@yahoo.com

†drmafzalansari@yahoo.com

model proposed by Udagawa and Tamura [12] explained the ICF in terms of the break-up of the projectile into α-clusters in the nuclear field of the target nucleus followed by fusion of one of the fragments with the target nucleus. The model uses distorted-wave Born approximation (DWBA) formalism of elastic break-up to calculate the shape of energy spectra and angular distribution of the projectile like fragments, but fails to give absolute cross section due to the lack of information about the spectroscopic form factors of the continuum states of the product nuclei. The PEP [13] and hot-spot models [14] are applicable only at much higher projectile energy. In the PEP model, the particles transferred from the projectile to the target nucleus are assumed to get accelerated in the nuclear field of the target nucleus and, hence, acquire extra velocity to escape. As a matter of fact, none of the above theoretical models are able to explain the gross features of experimental data available below 10 MeV/nucleon energy. Different methods have been employed for the study of ICF reactions, such as excitation function measurements, recoil range distributions of evaporation residues (ERs), velocity distribution of ERs, kinetic energy spectra and angular distribution studies of projectile like fragments (PLFs), and angular distribution measurement of ERs.

Recent measurements [15–22] of excitation functions (EFs) and recoil range distributions (RRDs) in the forward direction, etc., for a large number of evaporation residues produced in heavy-ion (HI) reactions in various projectile-target combinations have indicated the importance of CF and ICF processes at energies above the Coulomb barrier and below 10 MeV/nucleon. As a part of the ongoing program [22–26] to study the CF and ICF in heavy-ion reactions, this work has been undertaken and excitation functions for 18 evaporation residues produced in the ^{20}Ne + ^{59}Co system have been measured in the energy range ≈62–150 MeV, using the recoil-catcher technique followed by offline γ-spectroscopy. In these measurements, special care has been taken to remove the precursor decay contributions in the production of several evaporation residues to get the independent production cross sections of the residues. Measured EFs are then compared with the predictions of the statistical model code PACE-2 [27] and analyses of the results have been discussed. The dependence of incomplete fusion fraction with projectile energy has also been discussed. Moreover, entrance-channel mass-asymmetry dependence of the ICF fraction has been investigated and the results are discussed in Sec. IV.

II. EXPERIMENTAL DETAILS

A. Target preparation

Targets for irradiations were made by depositing specpure ^{59}Co by a vacuum evaporation technique on aluminum backing of ≈2 mg/cm^2 thickness. The thickness of each target was measured by two methods: (i) weighing individual aluminum foils before and after deposition of the target material and (ii) measuring the energy loss suffered by 5.486-MeV α particles from the ^{241}Am source, while traversing through the target material. The thickness of ^{59}Co deposited on the aluminum backing was lying between 37–187 μg/cm^2. The target foils were cut into pieces of 1.5 × 1.5 cm^2 and were pasted using the conducting glue zapon on aluminum holders of the standard size having concentric holes 10 mm in diameter. The aluminum holders of the same size were used to reproduce the target geometry and also rapid heat dissipation.

B. Irradiations

The experiment was performed at the Variable Energy Cyclotron Centre (VECC), Kolkata, India. Aluminum backing of ^{59}Co served as the energy degrader as well as the catcher to trap the recoiling residues produced during irradiations. Two stacks consisting of five targets each of ^{59}Co backed by 2 mg/cm^2 thick aluminum foils were bombarded with a ^{20}Ne^{+7} beam energy of ≈150 and 110 MeV. Irradiations were carried out to encompass the beam energy ranging from 62–150 MeV. Thus, the excitation functions of evaporation residues were measured at 10 beam energies for the projectile ^{20}Ne^{+7}. The irradiation time was ≈6 h. The weighted average beam current of about ≈60 nA behind the target assembly was measured with an electron suppressed Faraday cup, using a current integrator device. Details of the experimental setup used for irradiation have been given in our earlier Ref. [22]. The mean energy of the ^{20}Ne ion beam incident at half the thickness on each foil in the stack was calculated from the energy degradation of the incident beam energy, using stopping power and range calculation software SRIM-2006 [28]. The beam fluxes measured by two methods (time-weighted beam current and total charge collected in Faraday cup) are found to agree with each other within 10% variation. The inherent energy spread in the 150-MeV ^{20}Ne beam is 0.5 MeV.

C. Calibration of spectrometer and post irradiation analysis

After irradiation and cooling, the residual γ-activities produced in various targets along with their aluminum catcher foils were recorded using a 60-cm^3 HPGe detector, coupled to PC-based data acquisition system, at VECC, Kolkata. The distance between the irradiated sample and the detector was adjusted so that the dead time in recording was always less than 10%. The softwares MAESTRO [29] and FREEDOM [30] were used for data analysis. The resolution of the HPGe detector was found to be 1.9 keV at 1.33 MeV γ-rays of ^{60}Co. The geometry-dependent efficiencies of the HPGe detector at various source-detector distances (at which the irradiated targets were counted) were measured using the ^{152}Eu standard source of known strength. The evaporation residues were identified not only by their characteristic γ-ray energies, but also by their half-lives and branching ratios. The γ-ray energy spectra of individual target-catcher assembly were recorded at increasing times. A typical γ-ray energy spectrum obtained from the irradiated ^{59}Co target by the ^{20}Ne ion beam at ≈150 MeV beam energy is shown in Fig. 1. The area under the photopeaks of identified γ-rays of evaporation residues were used to estimate the counting rates followed by the production probability measurement. The spectroscopic data used for yield measurements such as γ-ray energies and their abundances and half-lives of evaporation residue, etc., were taken from the Table of Isotopes [31]. Identified evaporation

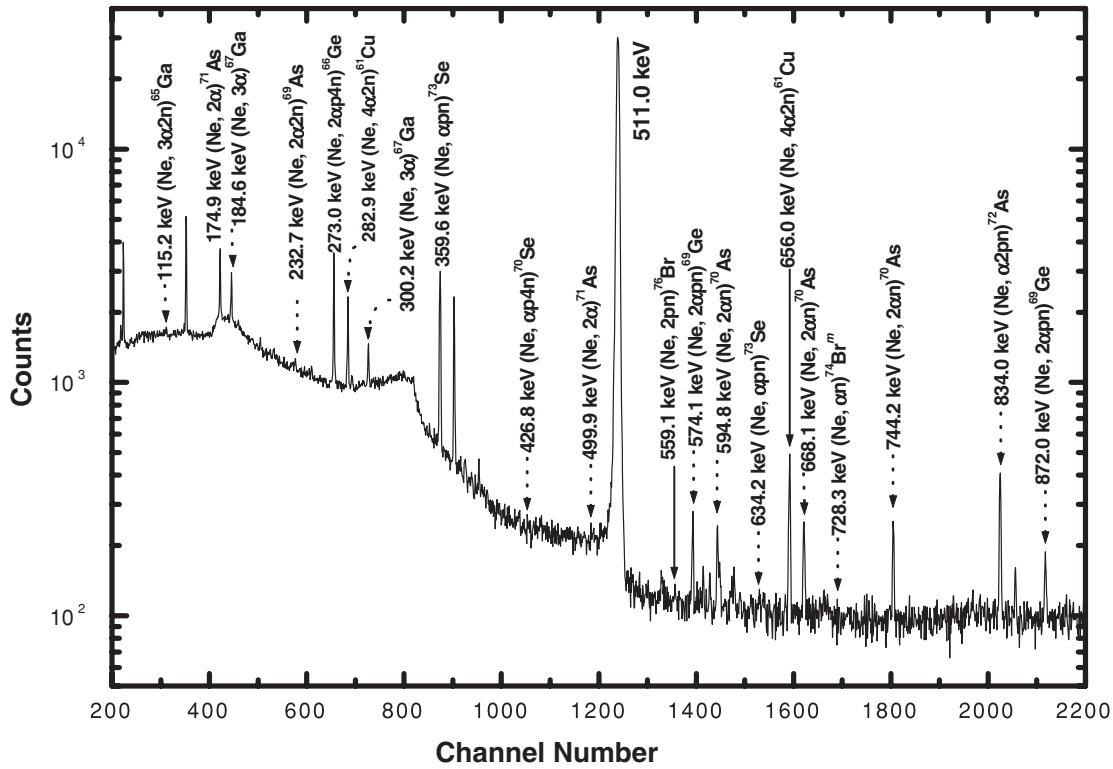

FIG. 1. Typical γ-ray energy spectrum obtained from the irradiation of ^{59}Co with ^{20}Ne beam at ≈150 MeV.

residues, along with their spectroscopic data used for yield measurements, are listed in Table I. The geometry-dependent efficiency (ε_G) of the detector for different source-detector separation distance was calculated using the relation

$$\varepsilon_G = S/[S_0 \exp(-\lambda_1 t)\theta_1] \quad (1)$$

where S is the observed disintegration rate of the γ-ray source ^{152}Eu at the time of measurement, S_0 is the absolute disintegration rate of the manufacture, λ_1 is the decay constant, t is the time lapsed between the date of manufacture of source and start of the counting, θ_1 is the branching ratio of the characteristic γ-ray of the source. A polynomial of degree 5 having the following form was found to give the best fit for these curves:

$$\varepsilon_G = a_0 + a_1 E + a_2 E^2 + a_3 E^3 + a_4 E^4 + a_5 E^5, \quad (2)$$

where the coefficients a_0, a_1, a_2, a_3, and a_5 have different values for different source-detector distances and E is the energy of the characteristic γ-rays. The experimentally measured reaction cross section $\sigma_\gamma(E)$ for a particular reaction product has been computed using the following expression [32]:

$$\sigma_r(E) = \frac{A\lambda \exp \lambda t_2}{N_0 \varphi \vartheta \varepsilon_G K[1 - \exp(-\lambda t_1)][1 - \exp(-\lambda t_3)]}, \quad (3)$$

where A is the total number of counts observed under the photopeak of characteristic γ-ray in time t_3, λ is the decay constant of the residual nucleus, N_0 is the total number of nuclei present in the target, ϕ is the incident ion beam flux, θ is the branching ratio of the identified γ-ray, ε_G is the geometry-dependent efficiency of the detector, t_1 is the irradiation time, t_2 is the time lapse between the end of irradiation and the start of counting and t_3 in the data collection time, and $K = [1 - \exp(-\mu d)]/\mu d$ is the correction for self-absorption of the γ-ray with the absorption coefficient μ for the target of thickness d. During the irradiation, a factor $[1 - \exp(-\lambda t_1)]$ takes care of the decay of the evaporation residue during irradiation time t_1 and is known as the saturation correction factor. The correction factor for the decay of the induced activity due to delay time t_2 between the end of irradiation and the start of counting is taken care of by $[\exp(-\lambda t_2)]$ and the correction factor due to the decay of the irradiated sample during data accumulation time t_3 is taken as$[1 - \exp(-\lambda t_3)]$. All the spectroscopic data that used cross-section measurements have been taken from Table of Isotopes [31]. The evaporation residues identified by their γ-ray energies and branching ratios, etc., are given in Table I. Excitation functions for 18 evaporation residues, ^{77}Kr (pn), ^{76}Kr ($p2n$), ^{76}Br ($2pn$), ^{75}Br (α), ^{74}Br (αn), ^{73}Se (αpn), ^{70}Se ($\alpha p4n$), ^{72}As ($\alpha 2pn$), ^{71}As (2α), ^{70}As ($2\alpha n$), ^{69}As($2\alpha 2n$), ^{69}Ge ($2\alpha pn$), ^{67}Ge ($2\alpha p3n$), ^{66}Ge ($2\alpha p4n$), ^{67}Ga (3α), ^{66}Ga ($3\alpha n$), ^{65}Ga ($3\alpha 2n$), and ^{61}Cu ($4\alpha 2n$), have been measured.

III. ESTIMATION OF INDEPENDENT CROSS SECTIONS FROM THE MEASURED CUMULATIVE CROSS SECTIONS

Some of the radioactive residues are produced independently in the interaction of ^{20}Ne with ^{59}Co (giving rise to independent yield), while some of them are also produced by the decay of their higher-charge isobar precursors through β^+ emission and/or by EC process (giving rise to cumulative yield). For such cases, cumulative cross sections have been

TABLE I. List of identified evaporation residues produced via complete and/or incomplete fusion and their spectroscopic data.

S. No.	Reactions	Half-life	E_γ (keV)	Branching ratio θ (%)
1.	^{59}Co(Ne, pn)^{77}Kr	1.24 *h*	129.8	80.0
2.	^{59}Co(Ne, $p2n$)^{76}Kr	14.8 *h*	315.7	39.0
			406.5	12.1
			452.0	9.8
3.	^{59}Co(Ne, $2pn$)^{76}Br	16.2 *h*	559.1	74.0
4.	^{59}Co(Ne, α)^{75}Br	1.62 *h*	286.6	92.0
5.	^{59}Co(Ne, αn)^{74m}Br	41.50 *m*	728.3	35.0
6.	^{59}Co(Ne, αpn)^{73}Se	7.15 *h*	359.6	97.0
			634.2	20.0
7.	^{59}Co(Ne, $\alpha p4n$)^{70}Se	41.1 *m*	426.8	28.8
8.	^{59}Co(Ne, $\alpha 2pn$)^{72}As	1.08 *d*	834.0	79.5
9.	^{59}Co(Ne, 2α)^{71}As	2.70 *d*	174.9	83.1
			499.9	20.8
10.	^{59}Co(Ne, $2\alpha n$)^{70}As	52.60 *m*	594.8	16.3
			668.1	21.2
			744.2	20.8
11.	^{59}Co(Ne, $2\alpha 2n$)^{69}As	15.1 *m*	232.7	10.9
12.	^{59}Co(Ne, $2\alpha pn$)^{69}Ge	1.62 *d*	574.1	13.3
			872.0	11.9
13.	^{59}Co(Ne, $2\alpha p3n$)^{67}Ge	18.70 *m*	167.0	84.0
14.	^{59}Co(Ne, $2\alpha p4n$)^{66}Ge	2.26 *h*	273.0	10.5
			381.9	28.2
15.	^{59}Co(Ne, 3α)^{67}Ga	3.26 *d*	184.6	20.4
			300.2	16.6
16.	^{59}Co(Ne, $3\alpha n$)^{66}Ga	9.49 *h*	1039.3	37.9
17.	^{59}Co(Ne, $3\alpha 2n$)^{65}Ga	15.20 *m*	115.2	55.0
18.	^{59}Co(Ne, $4\alpha 2n$)^{61}Cu	3.41 *h*	282.9	12.5
			656.0	10.7

measured if the half-life of the precursor is considerably smaller than that of the residue under investigation, by analyzing the induced activities at times greater than about seven to eight half-lives of the precursors. The cross section for commutative production of a given residue is the sum of (a) the cross section of its independent production and (b) the cross sections of independent production of its precursors multiplied by numerical coefficients, which may be greater than unity, proportional to the branching ratio for the decay of the precursors to the evaporation residue considered and depending on half-lives of the precursors and the evaporation residue. In such a case, the prescription given by Cavinato *et al.* [33] has been employed to separate the contribution from the precursor decay. If a precursor P is produced during irradiation with the cross section $\sigma^P_{\rm ind}$, which decays with half-life $T^P_{1/2}$, and the branching ratio P_P to a daughter nucleus D, the daughter nucleus D is also produced directly with cross section $\sigma^D_{\rm ind}$ during the irradiation and decays with half-life $T^D_{1/2}$, then the cumulative cross section $\sigma^D_{\rm cum}$ for the production of the daughter D in the sequential isobaric decay $P \rightarrow D$, is given by

$$\sigma^D_{\rm cum} = \sigma^D_{\rm ind} + F_P \sigma^P_{\rm ind}$$

The value of the precursor fraction F_P depends upon the branching ratio P_P of the precursor decay to the residues D and is given by

$$F_P = P_P \frac{T^D_{1/2}}{T^D_{1/2} - T^P_{1/2}}$$

Hence, the cumulative cross section of D is given by

$$\sigma^D_{\rm cum} = \sigma^D_{\rm ind} + P_P \frac{T^D_{1/2}}{T^D_{1/2} - T^P_{1/2}} \sigma^P_{\rm ind} \tag{4}$$

This procedure has been generalized to the case of successive decay of several precursor isobars produced in addition to the direct production of the residue. In the case of decay of two precursor isobars A and B produced in the beam interaction, i.e.

$$A \rightarrow B \rightarrow C$$

with branching ratios P_A and P_B, the cumulative cross section for the production of C has been obtained as [33]

$$\sigma^C_{\rm cum} = \sigma^C_{\rm ind} + P_B \frac{T^C_{1/2}}{\left(T^C_{1/2} - T^B_{1/2}\right)} \sigma^B_{\rm ind} + P_A P_B \frac{\left(T^C_{1/2}\right)^2}{\left(T^C_{1/2} - T^A_{1/2}\right)\left(T^C_{1/2} - T^B_{1/2}\right)} \sigma^A_{\rm ind} \tag{5}$$

The contributions of the precursor decays have been separated out from the measured cumulative cross section to get the independent cross section of a reaction by using Eqs. (4) and (5). Using the above expressions, the independent production cross sections of the residues ^{77}Kr, ^{76}Kr and ^{76}Br produced in the complete fusion channel via the reactions *pn*, *p*2*n* and 2*pn* and the independent production cross sections for the evaporation residues ^{75}Br (α), ^{74}Br (αn), ^{73}Se (αpn), ^{70}Se ($\alpha p4n$), ^{72}As ($\alpha 2pn$), ^{71}As (2α), ^{70}As ($2\alpha n$), ^{69}As($2\alpha 2n$), ^{69}Ge ($2\alpha pn$), ^{67}Ge ($2\alpha p3n$), ^{66}Ge ($2\alpha p4n$), ^{67}Ga (3α), ^{66}Ga ($3\alpha n$), ^{65}Ga ($3\alpha 2n$), and ^{61}Cu ($4\alpha 2n$) produced in incomplete fusion channels via α-particle(s) have also been obtained.

As a representative case, the evaporation residue ^{77}Kr (1.24 h) is produced via the ^{59}Co (Ne, *pn*) ^{77}Kr reaction by the complete fusion of ^{20}Ne with ^{59}Co followed by the evaporation of one proton and one neutron from the compound system ^{79}Rb. The same residue ^{77}Kr may also be populated by the electron capture (EC) and/ or β^+ decay process of the higher-charge precursor isobar ^{77}Rb (3.9 m) produced via the ^{59}Co (Ne, 2*n*) ^{77}Rb reaction. The cumulative cross sections of ^{77}Kr measured after the complete decay of precursor ^{77}Rb may have contributions from the decay of precursor isobar ^{77}Rb in addition to its direct production. The residue ^{77}Kr is identified by 128.1-keV γ-rays in its decays to ^{77}Br. The contribution due to the decay of precursor isobar ^{77}Rb to the residue ^{77}Kr has been separated from measured cumulative cross sections of ^{77}Kr using expression (4) based on the formulation given by Cavinato *et al.* [33]. In the present case, the expression reduces to the form

$$\sigma_{\rm cum}^{\rm meas}(^{77}{\rm Kr}) = \sigma_{\rm ind}^{\rm meas}(^{77}{\rm Kr}) + 1.055_{\rm ind}^{\rm PACE}(^{77}{\rm Rb}) \qquad (6)$$

Similarly, the independent cross sections for the residues ^{76}Kr (*p*2*n*) and ^{76}Br (2*pn*) have been deduced.

In another example, the evaporation residue ^{75}Br may be produced by the complete fusion of ^{20}Ne with ^{59}Co followed by the evaporation of two protons and two neutrons (or one α-particle) from the compound system ^{79}Rb. The evaporation residue ^{75}Br with 1.62 h half-life produced via the reaction ^{59}Co(Ne, α)^{75}Br may also be populated by the EC and/or β^+-decay process of the higher-charge precursor isobars, i.e. ^{75}Rb and ^{75}Kr. The measured cumulative cross sections of ^{75}Br may have contributions from the precursor isobars of ^{75}Rb (17 s) and ^{75}Kr (4.5 min) in addition to its direct production. The cross sections of precursor isobars ^{75}Rb and ^{75}Kr could not be measured separately owing to their short half-lives. However, the cumulative cross section for the production of ^{75}Br has been measured at times (more than 6–8 half-lives) after the complete decay of the precursors. This residue has been identified by 285.5-keV γ-rays in its decay. As such, the contribution due to the decay of the precursor isobars ^{75}Rb and ^{75}Kr to the residue ^{75}Br has been separated out using the Cavinato *et al.* formulation based expression (5). In the present case, the expression reduces to the form

$$\sigma_{\rm cum}^{\rm meas}(^{75}{\rm Br}) = \sigma_{\rm ind}^{\rm meas}(^{75}{\rm Br}) + 1.048\sigma_{\rm ind}^{\rm PACE}(^{75}{\rm Kr}) + 1.051\sigma_{\rm ind}^{\rm PACE}(^{75}{\rm Rb}) \qquad (7)$$

Similarly, the evaporation residue ^{67}Ga (3.26 d), produced via the reaction ^{59}Co(Ne, 3α)^{67}Ga, may also be produced by the EC process of the higher-charge precursor isobar ^{67}Ge (18.70 min) via the reaction ^{59}Co(Ne, 2$\alpha p3n$)^{67}Ge. In this case, the measured cross section of ^{67}Ga has contributions from the precursor decay in addition to the direct production of ^{67}Ga. The contribution due to the decay of precursor isobar ^{67}Ge to the evaporation residue ^{67}Ga has been separated out from cumulative contribution to get the independent yield for the production of ^{67}Ga using the Cavinato *et al.* prescription. The expression (4) in the present case reduces to the form

$$\sigma_{\rm cum}^{\rm meas}(^{67}{\rm Ga}) = \sigma_{\rm ind}^{\rm meas}(^{67}{\rm Ga}) + 1.004\sigma_{\rm ind}^{\rm meas}(^{67}{\rm Ge}) \qquad (8)$$

In a similar way, the independent production cross sections for the evaporation residues ^{77}Kr (*pn*), ^{76}Kr (*p*2*n*), ^{75}Br (α), ^{74}Br (αn), ^{73}Se (αpn), ^{70}As ($2\alpha n$), ^{69}Ge ($2\alpha pn$), ^{67}Ga (3α), and ^{66}Ga ($3\alpha n$) have also been deduced from the measured cumulative cross sections and their precursor contributions by using the expressions shown in Table II.

There are many factors responsible for the errors and uncertainty in the experimentally measured cross sections. The errors in the measured cross sections may be introduced because of the uncertainty in the determination of the efficiency of the detector, uncertainty in the determination of the number of nuclei presenting the target sample due to nonuniformity

TABLE II. Contributions of produced higher-charge isobars precursor decay and the expressions used for extraction of independent production cross sections from measured cumulative cross sections.

Residues	Measured cross sections	Expressions used for extraction of independent production cross sections
^{77}Kr	Independent	$\sigma_{\rm cum}^{\rm meas}(^{77}{\rm Kr}) = \sigma_{\rm ind}^{\rm meas}(^{77}{\rm Kr}) + 1.055\sigma_{\rm ind}^{\rm PACE}(^{77}{\rm Rb})$
^{76}Kr	Independent	$\sigma_{\rm cum}^{\rm meas}(^{76}{\rm Kr}) = \sigma_{\rm ind}^{\rm meas}(^{76}{\rm Kr}) + 1.007\sigma_{\rm ind}^{\rm PACE}(^{76}{\rm Rb})$
^{75}Br	Independent	$\sigma_{\rm cum}^{\rm meas}(^{75}{\rm Br}) = \sigma_{\rm ind}^{\rm meas}(^{75}{\rm Br}) + 1.048\sigma_{\rm ind}^{\rm PACE}(^{75}{\rm Kr}) + 1.051\sigma_{\rm ind}^{\rm PACE}(^{75}{\rm Rb})$
^{74}Br	Independent	$\sigma_{\rm cum}^{\rm meas}(^{74}{\rm Br}) = \sigma_{\rm ind}^{\rm meas}(^{74}{\rm Br}) + 1.383\sigma_{\rm ind}^{\rm PACE}(^{74}{\rm Kr})$
^{73}Se	Independent	$\sigma_{\rm cum}^{\rm meas}(^{73}{\rm Se}) = \sigma_{\rm ind}^{\rm meas}(^{73}{\rm Se}) + 1.008\sigma_{\rm ind}^{\rm PACE}(^{73}{\rm Br}) + 1.009\sigma_{\rm ind}^{\rm PACE}(^{73}{\rm Kr})$
^{71}As	Cumulative	$\sigma_{\rm cum}^{\rm meas}(^{71}{\rm As}) = \sigma_{\rm ind}^{\rm meas}(^{71}{\rm As}) + 1.001\sigma_{\rm ind}^{\rm PACE}(^{71}{\rm Se}) + 1.001\sigma_{\rm ind}^{\rm PACE}(^{71}{\rm Br})$
^{70}As	Independent	$\sigma_{\rm cum}^{\rm meas}(^{70}{\rm As}) = \sigma_{\rm ind}^{\rm meas}(^{70}{\rm As}) + \sigma_{\rm ind}^{\rm meas}(^{70}{\rm Se})$
^{69}Ge	Independent	$\sigma_{\rm cum}^{\rm meas}(^{69}{\rm Ge}) = \sigma_{\rm ind}^{\rm meas}(^{69}{\rm Ge}) + 1.006\sigma_{\rm cum}^{\rm meas}(^{69}{\rm As})$
^{67}Ga	Independent	$\sigma_{\rm cum}^{\rm meas}(^{67}{\rm Ga}) = \sigma_{\rm ind}^{\rm meas}(^{67}{\rm Ga}) + 1.004\sigma_{\rm ind}^{\rm meas}(^{67}{\rm Ge})$
^{66}Ga	Independent	$\sigma_{\rm cum}^{\rm meas}(^{66}{\rm Ga}) = \sigma_{\rm ind}^{\rm meas}(^{66}{\rm Ga}) + 1.324\sigma_{\rm ind}^{\rm meas}(^{66}{\rm Ge})$

TABLE III. The measured cross sections for the production of evaporation residues ^{76,77}Kr, ^{74,75,76}Br and ^{73}Se.

Lab Energy (MeV)	σ_{cum} (^{77}Kr) (mb)	σ_{ind} (^{77}Kr) (mb)	σ_{cum} (^{76}Kr) (mb)	σ_{ind} (^{76}Kr) (mb)	σ_{cum} (^{76}Br) (mb)	σ_{ind} (^{76}Br) (mb)
62.9 ± 1.0	113.1 ± 10.7	102.8 ± 10.7	72.7 ± 3.0	69.6 ± 3.0	107.2 ± 7.2	28.2 ± 1.9
75.2 ± 0.8	22.0 ± 2.1	20.2 ± 2.1	147.6 ± 4.9	139.2 ± 4.9	182.7 ± 12.3	62.1 ± 4.2
86.5 ± 0.8	0.5 ± 0.1	0.5 ± 0.1	45.2 ± 1.8	39.8 ± 1.8	96.8 ± 6.5	41.6 ± 2.8
97.1 ± 0.7	–	–	15.5 ± 0.7	13.7 ± 0.7	14.2 ± 1.0	6.1 ± 0.4
107.0 ± 0.7	–	–	1.9 ± 0.3	1.5 ± 0.3	2.3 ± 0.2	1.1 ± 0.1
116.3 ± 0.6	–	–	–	–	0.4 ± 0.1	0.2 ± 0.02
125.2 ± 0.6	–	–	–	–	–	–
133.8± 0.6	–	–	–	–	–	–
142.1± 0.6	–	–	–	–	–	–
150.2± 0.7	–	–	–	–	–	–
Lab Energy (MeV)	σ_{cum} (^{75}Br) (mb)	σ_{ind} (^{75}Br) (mb)	σ_{cum} (^{74}Br) (mb)	σ_{ind} (^{74}Br) (mb)	σ_{cum} (^{73}Se) (mb)	σ_{ind} (^{73}Se) (mb)
62.9 ± 1.0	–	–	46.7 ± 7.1	–	22.9 ± 1.3	19.2 ± 1.3
75.2 ± 0.8	91.3 ± 8.4	79.4 ± 8.4	62.2 ± 8.4	–	133.4 ± 7.3	126.5 ± 7.3
86.5 ± 0.8	174.9 ± 11.8	136.4 ± 11.8	108.2 ± 13.1	107.6 ± 13.1	141.0 ± 7.7	126.1 ± 7.7
97.1 ± 0.7	164.2 ± 15.7	124.2 ± 15.7	171.8 ± 17.8	169.3 ± 17.8	96.4 ± 5.3	88.1 ± 5.3
107.0 ± 0.7	84.3 ± 5.7	63.9 ± 5.7	210.6 ± 20.6	204.0 ± 20.6	68.2 ± 4.6	63.3 ± 4.6
116.3 ± 0.6	56.7 ± 3.9	50.4 ± 3.9	253.4 ± 24.8	245.9 ± 24.8	95.5 ± 5.2	88.3 ± 5.2
125.2 ± 0.6	13.4 ± 1.0	11.2 ± 1.0	141.2 ± 15.0	136.9 ± 15.0	77.2 ± 4.3	65.2 ± 4.3
133.8± 0.6	5.1 ± 0.6	4.9 ± 0.6	123.4 ± 12.9	119.7 ± 12.9	92.8 ± 5.1	81.0 ± 5.1
142.1± 0.6	1.8 ± 0.4	–	86.1 ± 14.3	84.7 ± 14.3	79.0 ± 4.3	69.1 ± 4.3
150.2± 0.7	0.7 ± 0.1	–	60.5 ± 9.1	60.0 ± 9.1	60.7 ± 4.2	54.1 ± 4.2

in the deposition of target material, and errors in the flux measurement due to the fluctuation in the beam current. The overall error from all these factors including statistical errors is found to be less than 20%. The errors associated with the spectroscopic data have not been taken into account because any revision in the spectroscopic data would permit an easy recalculation of the cross section in the future. A detailed discussion of the error analysis has been given in our earlier Ref. [23]. Experimentally measured cross sections for the production of various evaporation residues are tabulated in Tables III–V. To the best of our knowledge, no data is available for comparison of these measurements. The details of theoretical calculations and the parameters used are discussed in the following section.

The independent cross sections have been compared with the statistical model code PACE-2 [27], which uses Monte Carlo simulation procedure for the de-excitation of the compound nucleus and are found to agree well with the theoretical predictions. The optimization of input parameters has been done by achieving best fitting for the CF evaporation residues (*xn*/*pxn* channels), the details of the statistical model code PACE-2 and data analysis are discussed in Sec. IV.

IV. DATA ANALYSIS

A. Analysis of excitation functions using code PACE-2

In order to examine the equilibrated decay of the compound system ^{79}Rb produced in the interaction of the ^{20}Ne with the target ^{59}Co, measured excitations are compared with the statistical model code PACE-2 [27], which uses Monte Carlo simulation procedure for the de-excitation of the compound nucleus. This code is based on Hauser-Feshbach theory. The angular-momentum projections are calculated at each stage of de-excitation, which enables us to determine the angular distribution of emitted particles. The angular-momentum conservation is explicitly taken into account at each step that the CF cross sections are calculated using Bass formula [34].

For specific bombarding energy E, the partial cross section for the compound nucleus formation at angular momentum ℓ, is given by

$$\sigma_\ell = \pi\, \lambda\!\!\!^{-2}\, (2\ell + 1)\, T_\ell.$$

$\lambda\!\!\!^{-}$ is the reduced wavelength and T_ℓ is taken to be

$$T_\ell = [1 + \exp(\ell - \ell_{max}/\Delta)]^{-1},$$

where Δ is the diffuseness parameter and ℓ_{max} is determined by the total fusion cross section σ_F:

$$\sigma_F = \sum_{\ell=0}^{\infty} \sigma_\ell$$

The transmission coefficient for light particles n, p, and α emission are determined using the optical model potentials of Becchetti and Greenlees [35]. The γ-ray strength functions, required for $E1$, $E2$, and $M1$ transitions, may either be taken from default or taken from the tables of Endt [36]. In this code, level density parameter $a = A/K$ MeV^{-1} is one of the important parameters, where A is the mass number of the compound nucleus and K is called the level density parameter constant, which affects the equilibrium components. In this

TABLE IV. The measured cross sections for the production of evaporation residues ^{70}Se, ^{69,70,71,72}As, ^{66,67,69}Ge and ^{67}Ga.

Lab Energy (MeV)	σ_{ind} (^{70}Se) (mb)	σ_{ind} (^{72}As) (mb)	σ_{cum} (^{71}As) (mb)	σ_{cum} (^{70}As) (mb)	σ_{ind} (^{70}As) (mb)	σ_{ind} (^{69}As) (mb)
62.9 ± 1.0	1.5 ± 0.2	–	–	22.5 ± 2.5	21.0 ± 2.5	–
75.2 ± 0.8	10.5 ± 1.1	26.5 ± 2.5	13.4 ± 1.0	44.7 ± 4.7	34.2 ± 4.9	–
86.5 ± 0.8	12.3 ± 1.5	86.7 ± 4.8	59.4 ± 7.8	63.7 ± 4.4	51.4 ± 4.6	–
97.1 ± 0.7	15.7 ± 1.7	144.3 ± 8.0	96.7 ± 5.7	62.9 ± 3.7	47.2 ± 4.1	–
107.0 ± 0.7	21.2 ± 7.8	88.4 ± 8.4	131.9 ± 9.4	77.6 ± 3.8	56.4 ± 8.7	36.3 ± 6.8
116.3 ± 0.6	37.0 ± 4.6	96.1 ± 5.3	215.1 ± 12.4	162.7 ± 7.1	125.7 ± 8.5	51.1 ± 5.2
125.2 ± 0.6	42.3 ± 6.2	59.2 ± 3.4	179.8 ± 10.5	213.5 ± 8.6	171.2 ± 10.6	42.4 ± 4.3
133.8 ± 0.6	–	90.1 ± 5.0	144.1 ± 8.3	246.2 ± 8.0	–	39.6 ± 7.2
142.1 ± 0.6	–	67.1 ± 3.9	126.0 ± 7.4	118.1 ± 3.9	–	57.4 ± 10.2
150.2 ± 0.7	–	53.1 ± 3.3	86.5 ± 6.4	58.5 ± 2.4	–	46.4 ± 4.8

Lab Energy (MeV)	σ_{cum} (^{69}Ge) (mb)	σ_{ind} (^{69}Ge) (mb)	σ_{ind} (^{67}Ge) (mb)	σ_{ind} (^{66}Ge) (mb)	σ_{cum} (^{67}Ga) (mb)	σ_{ind} (^{67}Ga) (mb)
62.9 ± 1.0	–	–	–	–	–	–
75.2 ± 0.8	14.7 ± 2.5	–	–	–	–	–
86.5 ± 0.8	39.8 ± 2.3	–	–	–	10.2 ± 1.8	–
97.1 ± 0.7	107.7 ± 4.3	–	–	–	23.1 ± 3.1	–
107.0 ± 0.7	115.4 ± 6.7	79.1 ± 4.6	–	30.6 ± 3.1	39.8 ± 4.3	–
116.3 ± 0.6	146.7 ± 5.8	95.3 ± 3.8	28.4 ± 4.5	45.9 ± 3.5	118.0 ± 5.5	89.5 ± 4.2
125.2 ± 0.6	129.0 ± 5.1	86.3 ± 3.4	45.8 ± 5.1	56.5 ± 5.5	231.6 ± 9.8	185.6 ± 7.9
133.8 ± 0.6	120.6 ± 4.8	80.8 ± 3.2	61.2 ± 6.2	65.2 ± 6.5	271.2 ± 12.3	209.8 ± 9.5
142.1 ± 0.6	181.2 ± 7.9	123.4 ± 5.5	48.3 ± 5.0	60.5 ± 6.3	214.0 ± 9.2	165.5 ± 7.1
150.2 ± 0.7	160.1 ± 7.8	113.7 ± 5.5	40.8 ± 4.4	51.8 ± 5.8	327.7 ± 15.2	286.8 ± 13.3

code, most of the required input parameters have been used as default.

B. Interpretation of experimental results

The PACE-2 calculations are carried out for evaporation residues formed in CF and the parameters are optimized so as to reproduce the cross section of ERs produced exclusively in CF, e.g., *xn* and *pxn* products. With these parameters, the predicted CF cross sections for alpha emission products and lower mass ones are calculated. Any increase in the experimental cross section over the PACE-2 prediction is taken as a signature of ICF. Of course, the Q value for that ICF channel should be also high enough to corroborate the ICF formation of ER. The residues ^{77}Kr(pn) and ^{76}Kr($p2n$) are produced directly as well as in the decay mode of the produced higher-charge precursor isobars ^{77}Rb and ^{76}Rb, respectively. The independent cross sections for residues ^{77}Kr and ^{76}Kr have been deduced from the measured cumulative cross sections using expressions given in Table II. The measured cumulative cross sections of ^{76}Br produced in the reaction ^{59}Co(Ne, $2pn$)^{76}Br may have the contributions from the decay of its higher-charge precursor isobars ^{76}Rb and ^{76}Kr. The half-lives of ^{76}Br and its precursor ^{76}Kr are comparable (16.2 and 14.8 h, respectively). In such a case, the formulation developed in Ref. [37] has been followed and independent cross sections for the production of ^{76}Br have been obtained.

Reasonably good agreement is observed between the experimental and calculated cross section for ^{77}Kr(pn) and ^{76}Kr($p2n$), while in the case of ($2pn$) emission products (^{76}Br), the decay of ^{76}Kr to ^{76}Br could add uncertainties in

TABLE V. The measured cross sections for the production of evaporation residues ^{65,66}Ga and ^{61}Cu.

Lab Energy (MeV)	σ_{cum} (^{66}Ga) (mb)	σ_{ind} (^{66}Ga) (mb)	σ_{ind} (^{65}Ga) (mb)	σ_{ind} (^{61}Cu) (mb)
86.5 ± 0.8	112.7 ± 8.3	–	–	–
97.1 ± 0.7	88.1 ± 6.4	–	–	2.5 ± 0.5
107.0 ± 0.7	120.4 ± 12.0	80.0 ± 8.0	–	18.4 ± 3.6
116.3 ± 0.6	108.1 ± 7.6	47.3 ± 3.3	–	49.5 ± 8.0
125.2 ± 0.6	125.1 ± 12.5	50.3 ± 5.0	67.6 ± 7.1	45.9 ± 2.4
133.8 ± 0.6	161.9 ± 16.0	75.6 ± 7.5	54.5 ± 6.6	60.2 ± 2.6
142.1 ± 0.6	232.8 ± 23.1	152.7 ± 15.1	51.7 ± 6.1	94.5 ± 4.9
150.2 ± 0.7	261.7 ± 26.7	193.1 ± 19.5	59.2 ± 8.5	117.9 ± 5.0

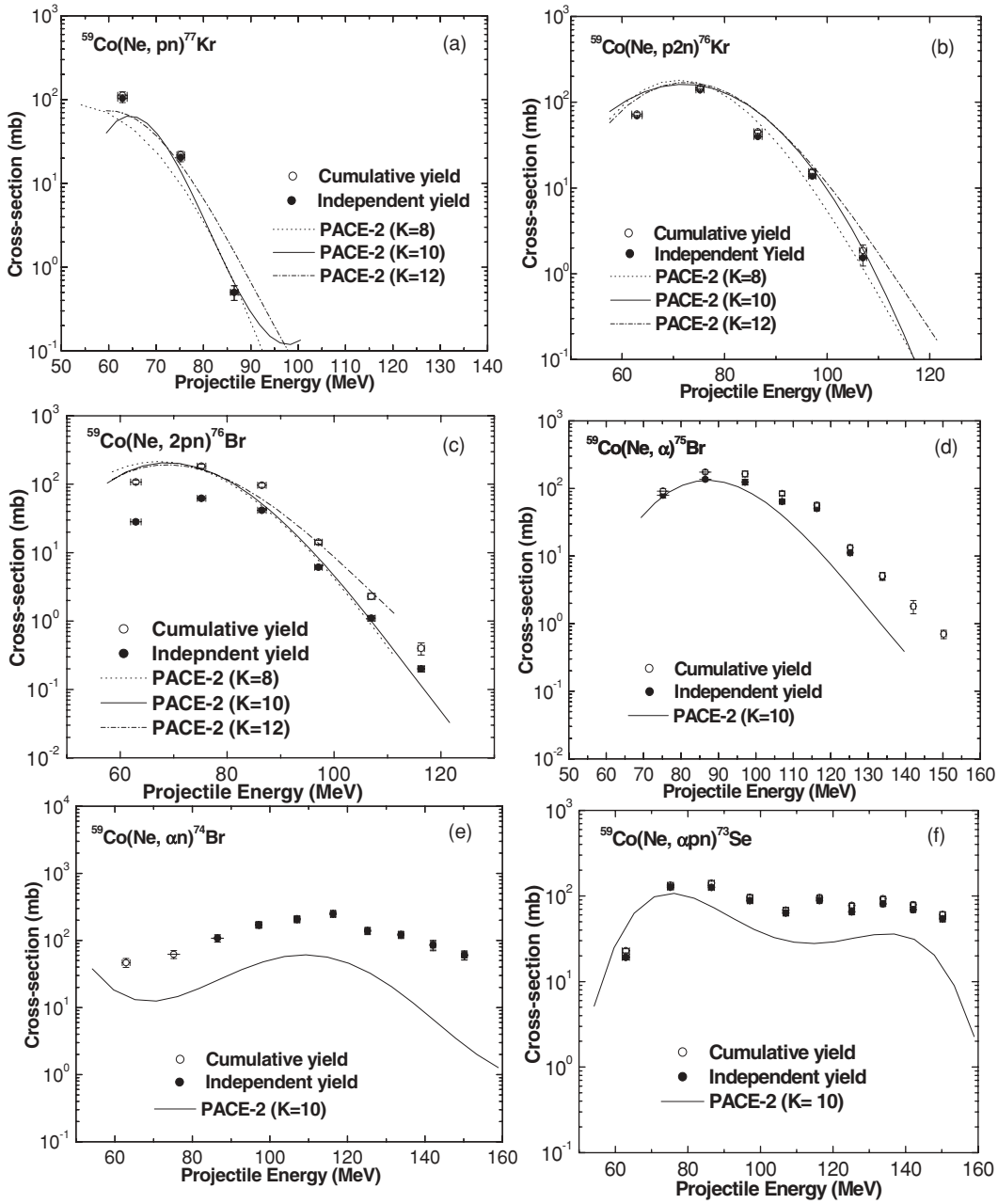

FIG. 2. Excitation functions of the evaporation residues ^{76,77}Kr, ^{74,75,76}Br and ^{73}Se produced in the ^{20}Ne + ^{59}Co reaction. Solid circles represent experimental data. The dotted, solid, and dashed-dotted lines represent the polynomial fit to the PACE-2 predictions at input parameter $K = 8$, 10 and 12.

the deduced cross sections at lower energies in adopting the formulation in Ref. [37]. Some appreciable yield contribution may arise due to the isomeric state decay of ^{76}Br, which has not been taken into account in Ref. [37]. This may cause lower extracted experimental cross-section values for the production of ^{76}Br at low projectile energies. Nevertheless, at higher beam energies, again reasonably good agreement has been observed. The measured cumulative and independent cross sections for the residues ^{77}Kr, ^{76}Kr and ^{76}Br have been plotted in Figs. 2(a), 2(b) and 2(c), respectively. The PACE-2 parameters are optimized by reproducing the cross sections of pure CF products and it is assumed that the CF cross sections of the ERs produced by both CF and ICF are correct. With this assumption, the ICF cross sections are deduced by subtracting the PACE-2 CF cross sections from the experimental data to deduce the ICF cross sections. As the agreement between the experimental and calculated CF cross section are within 50%, the ICF cross sections deduced by the above procedure will have an error of this order.

The effect of variation of parameter K (= 8, 10, 12) on the calculated EFs for the evaporation residues produced in the reactions ^{59}Co(Ne, pn)^{77}Kr, ^{59}Co(Ne, $p2n$)^{76}Kr, and ^{59}Co(Ne, $2pn$)^{76}Br are also shown in these figures by dotted, solid and dashed-dotted lines, respectively. It is quite clear from these

figures that PACE-2 predictions corresponding to the level density parameter constant $K = 10$ reproduce the measured EFs satisfactorily, in general, and these reaction channels populated via the complete fusion (CF) process, as there is no α particle(s) in the exit channel. Using $K = 10$, i.e. level density parameter $A/10$, theoretical EFs for the evaporation residues ^{75}Br (α), ^{74}Br (αn), ^{73}Se (αpn), ^{70}Se ($\alpha p4n$), ^{72}As ($\alpha 2pn$), ^{71}As (2α), ^{70}As ($2\alpha n$), ^{69}As($2\alpha 2n$), ^{69}Ge ($2\alpha pn$), ^{67}Ge ($2\alpha p3n$), ^{66}Ge ($2\alpha p4n$), ^{67}Ga (3α), ^{66}Ga ($3\alpha n$), ^{65}Ga ($3\alpha 2n$), and ^{61}Cu ($4\alpha 2n$) associated with α-particle(s) emission channels and expected to be produced through the incomplete fusion process (where as it is assumed that the breakup of the projectile ^{20}Ne into α + ^{16}O or ^{8}Be + ^{12}C fragments and fusion of one of the fragments with the target takes place) are calculated and displayed in Figs. 2(d)–2(f), 3(a)–3(f) and 4(a)–4(f), along with the measured independent cross-section values.

The independent cross sections of the residues ^{75}Br, ^{74}Br, and ^{73}Se produced in 1α-emission channels in the reactions ^{59}Co(Ne, α)^{75}Br, ^{59}Co(Ne, αn) ^{74}Br, and ^{59}Co(Ne, αpn)^{73}Se have also been separated out from their measured cumulative cross sections, using the expressions given in Table II. On the other hand, independent cross sections for the residue ^{70}Se produced in the reaction ^{59}Co(Ne, $\alpha p4n$) ^{70}Se have been measured and no precursor contribution has been found. Measured EF for the residue ^{72}As, produced in the reaction ^{59}Co(Ne, $\alpha 2pn$)^{72}As, is also independent as its higher-charge precursor isobar ^{72}Se is a very long-lived nuclide. For the residues ^{75}Br, ^{74}Br, and ^{73}Se, measured cumulative and independent cross sections are obtained and are displayed, while for the residues ^{70}Se and ^{72}As, only measured independent cross sections are displayed along with their theoretical values in Figs. 2(d)–2(f) and Figs. 3(a) and 3(b). Measured EFs associated with 1α-emission channels are found to be consistently higher in general than PACE-2 predictions, thereby indicating the presence of the ICF component along with CF. It is assumed that the ICF of the fragment ^{16}O (if ^{20}Ne undergoes breakup into fragments ^{16}O and ^{4}He) with the target ^{59}Co and subsequent emission of neutron and/or protons take place from the composite system, in addition to the CF of projectile ^{20}Ne with the target ^{59}Co followed by evaporation of nucleons and α particle from the compound system. The fragment ^{4}He, however, moves in a forward direction. It is worth mentioning repeatedly that the code PACE-2 does not take into account the ICF contribution, hence, the enhancement in the cross sections for the evaporation residues ^{75}Br (α), ^{74}Br (αn), ^{73}Se (αpn), ^{70}Se ($\alpha p4n$), and ^{72}As ($\alpha 2pn$) may be a ttributed to the ICF process of the type

$$^{20}\mathrm{Ne}(^{16}\mathrm{O} + {}^{4}\mathrm{He}) + {}^{59}\mathrm{Co} \rightarrow {}^{16}\mathrm{O} + {}^{59}\mathrm{Co}$$
$$\Rightarrow {}^{75}\mathrm{Br}^{*} + {}^{4}\mathrm{He} \quad (\alpha \text{ particle as spectator}).$$

Measured EFs for the reactions ^{59}Co(Ne, 2α)^{71}As, ^{59}Co(Ne, $2\alpha n$)^{70}As, ^{59}Co(Ne, $2\alpha 2n$)^{69}As, ^{59}Co(Ne, $2\alpha pn$)^{69}Ge, ^{59}Co(Ne, $2\alpha p3n$)^{67}Ge, and ^{59}Co(Ne, $2\alpha p4n$)^{66}Ge produced in various 2α-emission channels are shown in Figs. 3(c)–3(f) and Figs. 4(a) and 4(b). The measured cumulative cross sections for the evaporation residue ^{71}As, produced in the reaction ^{59}Co(Ne, 2α)^{71}As, have been compared directly with PACE-2 cumulative cross sections. Independent production cross sections for the residue ^{70}As, produced in the reaction ^{59}Co(Ne, $2\alpha n$)^{70}As, have been deduced from the measured cumulative cross sections, using the expressions given in Table II. In the measured EF for the residue ^{69}As, produced in the reaction ^{59}Co(Ne, $2\alpha 2n$)^{69}As, no precursor contribution from ^{69}Se has been noticed, hence, the measured EF for ^{69}As is also independent. Moreover, from the measured cumulative cross sections of residue ^{69}Ge, produced in the reaction ^{59}Co(Ne, $2\alpha pn$)^{69}Ge, its independent production cross section has been obtained using the expressions given in Table II. In the measured EFs of residues ^{67}Ge and ^{66}Ge, produced in the reactions ^{59}Co(Ne, $2\alpha p3n$)^{67}Ge and ^{59}Co(Ne, $2\alpha p4n$)^{66}Ge, no precursor contributions have been observed, hence, measured EFs correspond to independent cross sections. Comparison of measured EFs for the residues ^{71}As, ^{70}As, ^{69}As, ^{69}Ge, ^{67}Ge, and ^{66}Ge, produced in the reactions ^{59}Co(Ne, 2α)^{71}As, ^{59}Co(Ne, $2\alpha n$)^{70}As, ^{59}Co(Ne, $2\alpha 2n$)^{69}As, ^{59}Co(Ne, $2\alpha pn$) ^{69}Ge, ^{59}Co(Ne, $2\alpha p3n$)^{67}Ge and ^{59}Co(Ne, $2\alpha p4n$) ^{66}Ge with PACE-2 predictions, are shown in Figs. 3(c)–3(f) and Figs. 4(a)–4(b). More substantial enhancements in the experimental values than those in the PACE-2 predictions have been observed. These enhancements may be attributed to the fact that these residues may be populated not only by CF of ^{20}Ne with ^{59}Co but may have significant contributions from the ICF process (if the projectile ^{20}Ne breaks up into fragments ^{12}C and ^{8}Be and the fragment ^{12}C fuses with the target). Subsequent emission of neutrons and protons during de-excitation of the composite system leads to the production of the above residues populated through the ICF process.

The enhancement in the cross sections of the reaction products ^{71}As(2α), ^{70}As($2\alpha n$), ^{69}As(2α), ^{69}Ge($2\alpha pn$), ^{67}Ge($2\alpha p3n$), and ^{66}Ge($2\alpha p4n$) may be attributed to the incomplete fusion process of the type

$$^{20}\mathrm{Ne}\,(^{12}\mathrm{C} + {}^{8}\mathrm{Be}) + {}^{59}\mathrm{Co} \rightarrow {}^{12}\mathrm{C} + {}^{59}\mathrm{Co}$$
$$\Rightarrow {}^{71}\mathrm{As}^{*} + {}^{8}\mathrm{Be}\ ({}^{8}\mathrm{Be} \text{ as spectator}).$$

Excitation functions for the evaporation residues ^{67}Ga, ^{66}Ga, ^{65}Ga, and ^{61}Cu produced in 3α, $3\alpha n$, $3\alpha 2n$ and $4\alpha 2n$ emission channels along with PACE-2 predictions are shown in Figs. 4(c)–4(f). The residues ^{67}Ga and ^{66}Ga are produced via two different channels, directly and through the β^{+} decay of higher-charge precursor isobars ^{67}Ge and ^{66}Ge, respectively. The residue ^{67}Ga may be populated via two different channels: (i) complete fusion of ^{20}Ne with ^{59}Co, i.e., ^{20}Ne + ^{59}Co $\rightarrow$ ^{79}Rb* + 3α, and (ii) through the β^{+} decay of higher-charge isobar precursor ^{67}Ge(18.7 min) to ^{67}Ga (3.26 d), i.e.,

$$^{20}\mathrm{Ne} + {}^{59}\mathrm{Co} \Rightarrow {}^{67}\mathrm{Ge}^{*} + {}^{8}\mathrm{Be} + p + 3n,$$
$$^{67}\mathrm{Ge}^{*} \rightarrow {}^{67}\mathrm{Ga} + \beta^{+}.$$

Similarly, the residue ^{66}Ga may also be populated via two different channels: (i) complete fusion of ^{20}Ne with ^{59}Co, i.e., ^{20}Ne + ^{59}Co $\Rightarrow$ ^{79} Rb* + 3α + n, and (ii) through the β^{+} decay of higher-charge isobar precursor ^{66}Ge (2.3 h) to ^{66}Ga (9.5 h), i.e.,

$$^{20}\mathrm{Ne} + {}^{59}\mathrm{Co} \Rightarrow {}^{66}\mathrm{Ge}^{*} + {}^{8}\mathrm{Be} + p + 4n,$$
$$^{66}\mathrm{Ge}^{*} \rightarrow {}^{66}\mathrm{Ga} + \beta^{+}.$$

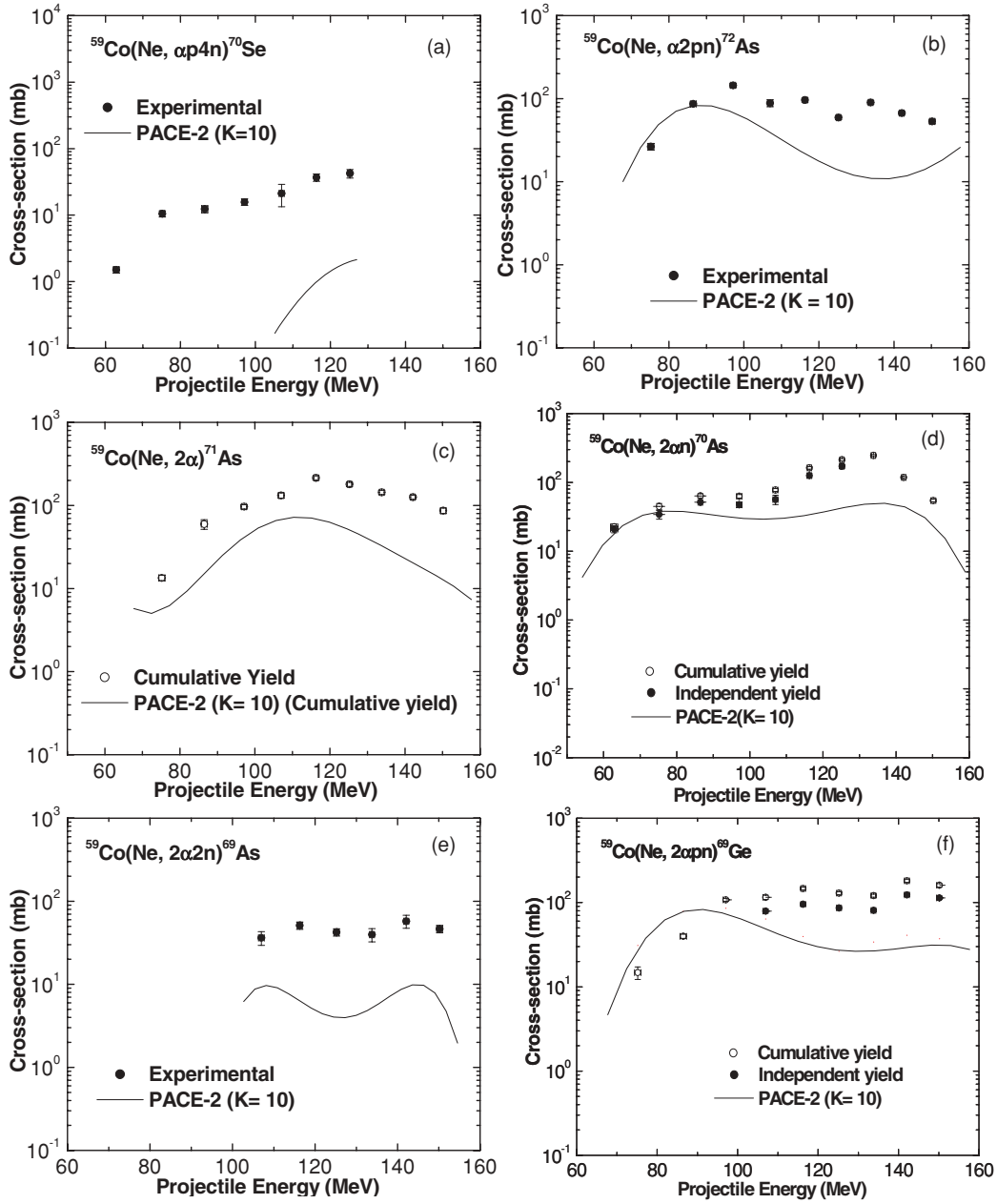

FIG. 3. Excitation function of the evaporation residues ^{70}Se, ^{69,70,71,72}As and ^{69}Ge produced in the ^{20}Ne + ^{59}Co reaction. Solid circles represent experimental data and solid lines represent the polynomial fit to the PACE-2 predictions at input parameter $K = 10$.

The measured cumulative and independent cross sections are displayed in Figs. 4(c) and 4(d). In the measured EFs for the residues ^{65}Ga and ^{61}Cu, no precursor contributions from ^{65}Ge and ^{61}Zn have been noticed. So, the measured independent cross sections for the residues ^{65}Ga and ^{61}Cu are displayed in Figs. 4(e)–4(f). It is seen from Figs. 4(c)–4(f) that substantial enhancements in the measured EFs over PACE-2 predictions have been observed. The enhancement may be attributed to the fact that these residues may be populated not only by the CF of projectile ^{20}Ne with target ^{59}Co, but may also have significant contributions from the ICF process. This may again be understood in the breakup of projectile ^{20}Ne into fragments ^{12}C + ^{8}Be (2α) or ^{4}He + ^{16}O and fusion of fragment ^{8}Be or ^{4}He with the target ^{59}Co, followed by emission of neutrons during de-excitation of the composite system. The enhanced measured cross sections for the ERs ^{65}Ga may be attributed to incomplete fusion process of the type

$$^{20}\mathrm{Ne}\,(^{8}\mathrm{Be} + {}^{12}\mathrm{C}) + {}^{59}\mathrm{Co} \rightarrow {}^{8}\,\mathrm{Be} + {}^{59}\mathrm{Co}$$
$$\Rightarrow {}^{67}\,\mathrm{Ga}^{*} + {}^{12}\mathrm{C} \quad ({}^{12}\mathrm{C}\text{ as spectator}),$$

while the enhanced cross sections for the residue ^{61}Cu may be attributed to the incomplete fusion process of the type

$$^{20}\mathrm{Ne}\,(^{4}\mathrm{He} + {}^{16}\mathrm{O}) + {}^{59}\,\mathrm{Co} \rightarrow {}^{4}\,\mathrm{He} + {}^{59}\mathrm{Co}$$
$$\Rightarrow {}^{63}\,\mathrm{Cu}^{*} + {}^{16}\mathrm{O} \quad ({}^{16}\mathrm{O}\text{ as spectator}).$$

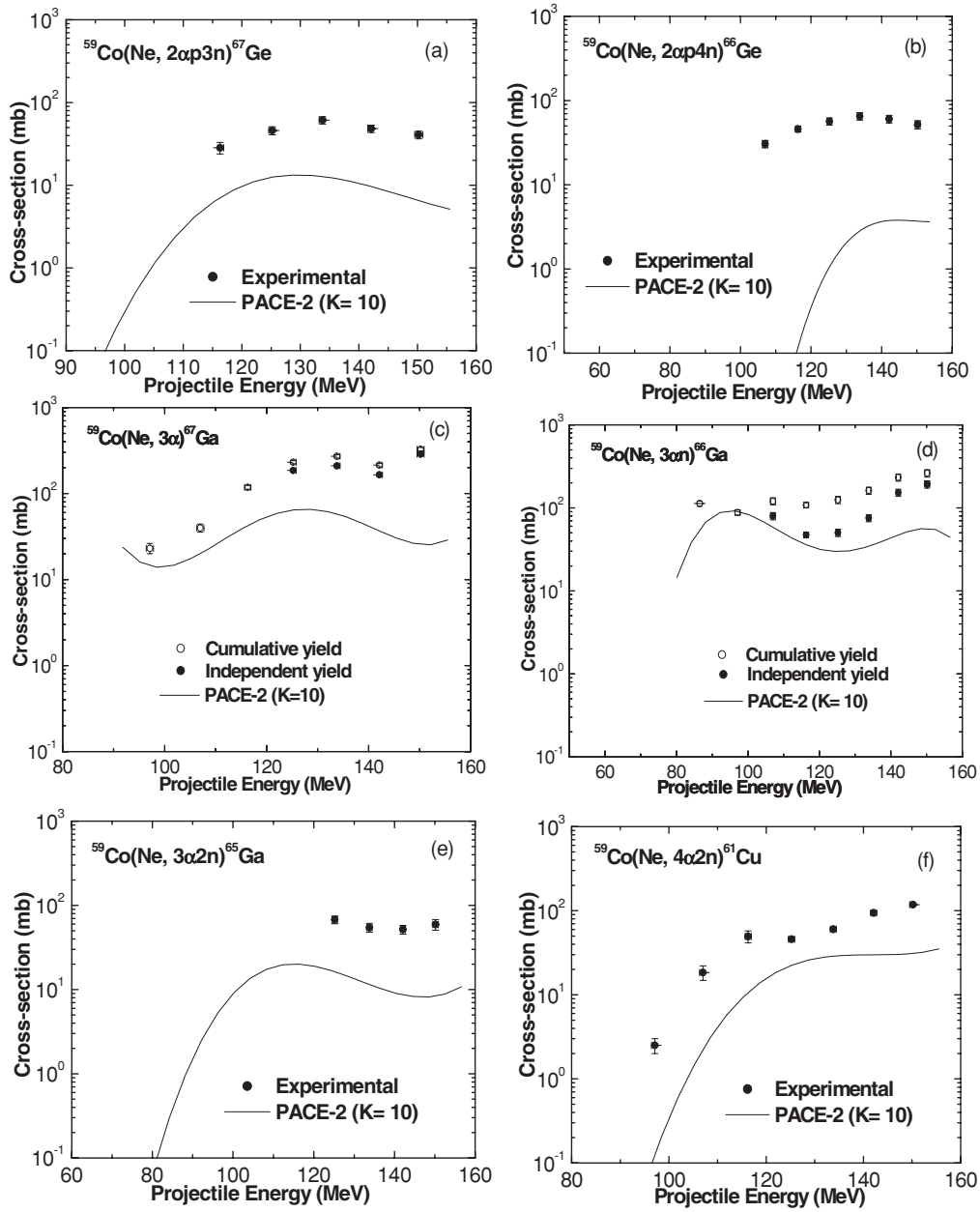

FIG. 4. Excitation function of the evaporation residues ^{66,67}Ge, ^{65,66,67}Ga and ^{61}Cu, produced in the ^{20}Ne + ^{59}Co reaction. Solid circles represent experimental data and solid lines represent the polynomial fit to the PACE-2 predictions at input parameter $K = 10$.

Finally, it is concluded from this analysis that evaporation residues ^{77}Kr, ^{76}Kr, and ^{76}Br are produced by the complete fusion (CF) process of the projectile while residues ^{75}Br, ^{74}Br, ^{73}Se, ^{70}Se, ^{72}As, ^{71}As, ^{70}As, ^{69}As, ^{69}Ge, ^{67}Ge, ^{66}Ge, ^{67}Ga, ^{66}Ga, ^{65}Ga, and ^{61}Cu populated in α-particle(s) emission channels are produced by the incomplete fusion (ICF) process of the projectile with the target.

C. Sum rule model calculations of the ICF

The sum rule model [11] based on the generalized concept of critical angular momentum proposed by Wilczynski *et al.* explained that the different ICF channels are populated in the angular-momentum space above the critical angular momentum for CF. The model predicted the ICF cross sections at projectile energies above 10.5 MeV/nucleon. This model predicts a very specific localization of the various reactions in ℓ-space. According to the sumrule model calculation, it is assumed that the ICF channels open only for those partial waves, which have ℓ values greater than $\ell_{\rm crit}$, i.e., ($\ell \geqslant \ell_{\rm crit}$). On the other hand, partial waves with $\ell \leqslant \ell_{\rm crit}$ contribute to the CF process. In this paper, we have made an attempt to calculate the cross sections for the CF and ICF channels for ERs formed during the fusion of the fragments of projectile ^{20}Ne with target ^{59}Co, using the sumrule model. The model contains three important free input parameters, namely, the temperature of the contact zone between the

TABLE VI. Typical sum-rule-model calculations and measured ICF cross sections at 107-MeV projectile energy.

Residues	σ_{exp} (mb)	σ_{PACE} (mb)	Difference (Experimental) σ_{ICF} (mb)	Transfer yield $\sigma_{sumrule}$ (mb)
PLFs (1α-emission channels)				
^{75}Br	63.9	38.6	25.2	
^{74}Br	204.0	69.4	134.6	
^{73}Se	63.3	25.7	37.6	
^{70}Se	21.2	0.24	21.0	
^{72}As	88.4	43.3	45.1	
		Total 1α-transfer yield	263.5	57
PLFs (2α-emission channels)				
^{71}As	131.9*	65.4*	66.4	
^{70}As	56.4	24.9	31.4	
^{69}As	36.3	9.4	26.9	
^{69}Ge	79.1	54.3	24.8	
^{66}Ge	30.6	–	30.6	
		Total 2α-transfer yield	180.1	7
PLFs (3α-emission channels)				
^{67}Ga	39.8	18.6	21.2	
^{66}Ga	80	65.9	14.1	
		Total 3α-transfer yield	35.3	17
PLFs (4α-emission channels)				
^{61}Cu	18.4		2.6	
		Total 4α-transfer yield	2.6	54
		Total transfer yield	**494.7**	**135**

*Cumulative cross-Section.

interacting partners (T), the diffuseness parameter (Δ) of transmission probability distribution (T_ℓ), and the Coulomb interaction radius (R_e). These parameters were taken as 3.5 MeV, 1.7$\hbar$, and 9.91 fm, respectively, as suggested by Wilczynski *et al.* [11]. Cross sections calculated by the sumrule model along with the measured ICF cross sections of various evaporation residues at a typical projectile energy $\approx$107 MeV (i.e., 5.3 MeV/nucleon) for the present system is listed in Table VI.

It can be seen from this table that the cross sections predicted by the sumrule model at projectile energy $\sim$5 MeV/nucleon are, in general, lower than the measured ICF cross sections. Since measured evaporation residues may have contributions from different target like products formed immediately after incomplete fusion, therefore, the total cross sections for the ICF reaction involving fusion of ^{16}O with ^{59}Co have been compared with those cross sections calculated from the sumrule model and so on for other channels. This is based on the assumption that the target like products formed after incomplete fusion de-excite by neutron, proton, and gamma-ray emission. As mentioned above, the sumrule predicted cross sections are lower than the measured ICF cross section. This indicates that ICF channels open only above ℓ_{crit} may not be applicable at lower projectile energies. Instead, ICF appears to complete with CF at lower ℓ values at lower projectile energies. Finally, it can also be observed from Table VI (last row) that the sum-rule calculations account for only 28% of the experimental ICF cross section at this projectile energy. Earlier, Singh *et al.* [19], Babu *et al.* [38], and Ali *et al.* [26] have also observed the similar anomalies when comparing their measured values with the sumrule model predictions at about 6 MeV/nucleon energy for the systems ^{16}O + ^{159}Tb, ^{16}O + ^{169}Tm, ^{13}C + ^{181}Ta, and ^{20}Ne + ^{55}Mn. One of the possible reasons for the disagreement in ICF reaction channels may be the non-validity of the generalized concept of critical angular momentum at projectile energy below 8 MeV/nucleon. In the sumrule model, incomplete fusion cross sections are negligibly small for l-waves close to or lower than critical angular momentum for complete fusion.

D. Incomplete fusion fraction and mass-asymmetry effect

An attempt has been made to estimate the ICF cross sections and the dependence of incomplete fusion fraction on the projectile energy and entrance-channel mass-asymmetry for the present ^{20}Ne + ^{59}Co system has been investigated.

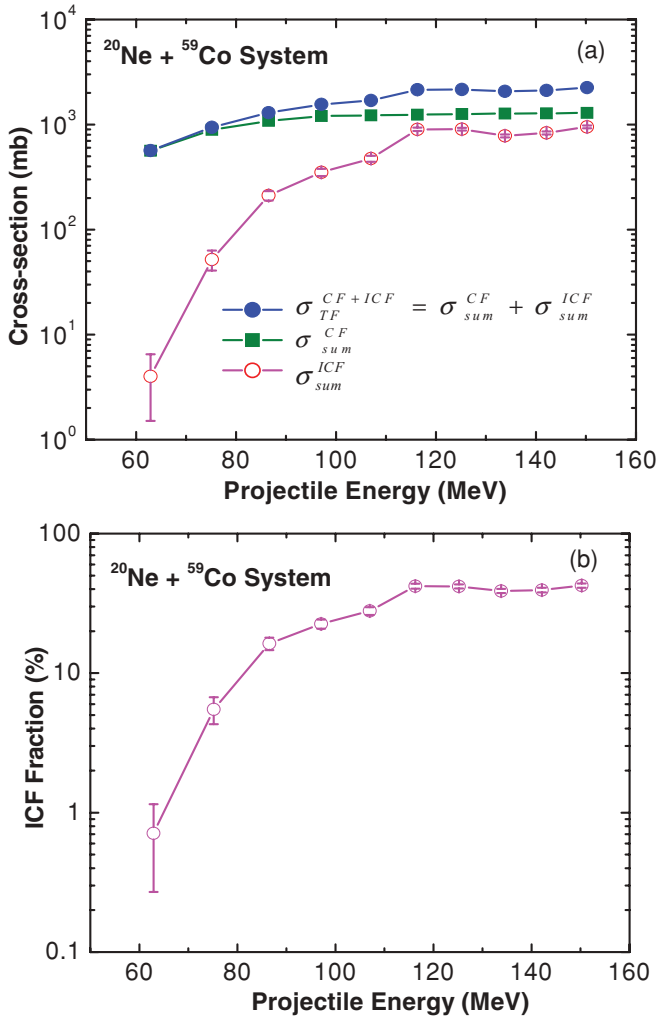

FIG. 5. (Color online) (a) Total fusion cross section ($\sigma_{\rm TF}^{\rm CF+ICF} = \sigma_{\rm sum}^{\rm CF} + \sigma_{\rm sum}^{\rm ICF}$) along with the sum of complete fusion (CF) cross sections ($\sigma_{\rm sum}^{\rm CF}$) and sum of incomplete fusion (ICF) cross sections ($\sigma_{\rm sum}^{\rm ICF}$) at different projectile energy for the system ^{20}Ne + ^{59}Co. (b) The ICF fraction as a function of projectile energy.

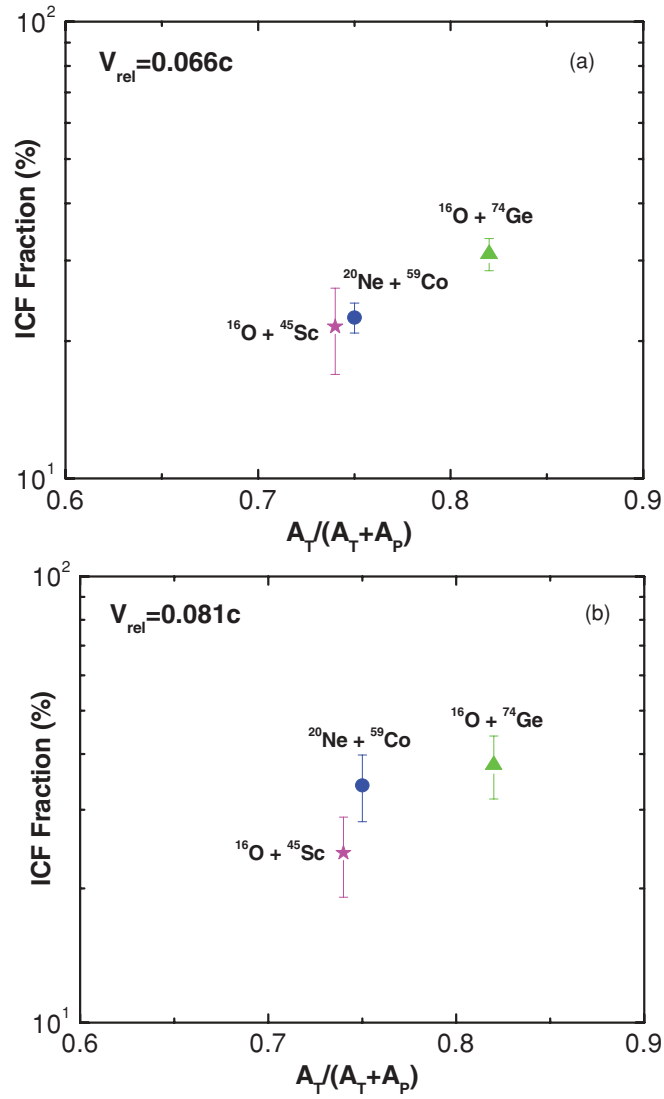

FIG. 6. (Color online) The ICF fraction as a function of entrance-channel mass-asymmetry at relative velocities (a) $V_{\rm rel} = 0.066c$ and (b) $V_{\rm rel} = 0.081c$ for different projectile-target systems.

The production cross sections, which have been measured experimentally, may be attributed to the both complete and/or incomplete fusion. As already mentioned, the enhancement in the experimentally measured production cross sections over the PACE-2 predictions in some of the residues may be attributed to the incomplete fusion process. As such, the ICF contribution ($\sigma^{\rm ICF}$) for individual channels has been estimated by subtracting the theoretically calculated complete fusion cross section by PACE-2 from the experimentally measured cross sections at each projectile energy. The total incomplete fusion cross section ($\sigma_{\rm sum}^{\rm ICF}$) was obtained by adding the incomplete fusion cross sections of different measured evaporation residues at each projectile energy. The total complete fusion cross section ($\sigma_{\rm sum}^{\rm ICF}$) was calculated using the code PACE-2 at each projectile energy. The total fusion cross section $\sigma_{\rm TF}^{\rm CF+ICF}$ was obtained by adding $\sigma_{\rm sum}^{\rm CF}$ and $\sigma_{\rm sum}^{\rm ICF}$. In Fig. 5(a), plots of $\sigma_{\rm sum}^{\rm CF}$, $\sigma_{\rm sum}^{\rm ICF}$ and $\sigma_{\rm TF}^{\rm CF+ICF}$ for the ^{20}Ne + ^{59}Co system are shown as a function of projectile energy. It has been observed that the ICF contribution increases with respect to the CF process as the projectile energy is increased. This may be understood with the fact that, as the projectile energy increases, the probability of the breakup of incident projectile into α clusters (i.e., breakup of ^{20}Ne into ^{16}O + α and/or ^{12}C + ^{8}Be) increases.

A ratio of incomplete fusion cross section to the total fusion cross section [$\sigma_{\rm ICF}/\sigma_{\rm (ICF+CF)}$] has been deduced and plotted as a function of projectile energy for the present system ^{20}Ne + ^{59}Co as shown in Fig. 5(b). It is observed from the figure that the ICF fraction invariably increases with projectile energy. The ICF fractions for the present system ^{20}Ne + ^{59}Co along with previously measured systems ^{16}O + ^{45}Sc [23,25] and ^{16}O + ^{74}Ge [24,25] as a function of mass-asymmetry for the same relative velocity $V_{\rm rel} = 0.066c$ and $V_{\rm rel} = 0.081c$ have been calculated and plotted in Figs. 6(a) and 6(b). Being different Coulomb barriers for the above-mentioned three different systems, the following expression, due to Morgenstern *et al.*

[8], has been used for the calculation of relative velocity

$$V_{\rm rel} = [\sqrt{2(E_{\rm CM} - E_{\rm CB})/\mu}] \quad (9)$$

where μ is the reduced mass of the system, $E_{\rm CM}$ is the center-of-mass energy, and $E_{\rm CB}$ is the Coulomb barrier. This expression takes into account the difference in the Coulomb barrier between each two projectile-target systems. It has been observed from the Figs. 6(a) and 6(b) that the ICF fraction increases with mass-asymmetry of the projectile-target systems. The present measurements suggest that ICF probability increases with mass-asymmetry of the interacting partner and supports the findings of previous work by Morgenstern *et al.* [8], Chakrabarty *et al.* [10], and Singh *et al.* [19]. However, a large number of data is needed to have a better understanding of such an observation and its dependence on nuclear structure effect.

V. SUMMARY AND CONCLUSIONS

Excitation functions of 18 evaporation residues produced in complete and/or incomplete fusion process have been measured in the ^{20}Ne + ^{59}Co system in the energy range ≈62–150 MeV. An attempt has been made to deduce the independent production cross sections from the measured cumulative cross sections and precursor decay contributions of different radio nuclides. The experimentally measured excitation functions have been compared with PACE-2 predictions, after correcting the precursor contributions. It has been observed that EFs for the residues produced through complete fusion channels ^{77}Kr (pn) and ^{76}Kr ($p2n$) are reproduced reasonably well with PACE-2 predictions, while in the case of the CF product ^{76}Br ($2pn$), the decay of ^{76}Kr to ^{76}Br could add uncertainties in the deduced cross sections at lower energies. Nevertheless, at higher beam energies, again reasonably good agreement has been observed. The evaporation residues produced in the incomplete fusion channels ^{75}Br (α), ^{74}Br (αn), ^{73}Se (αpn), ^{70}Se ($\alpha p4n$), ^{72}As ($\alpha 2pn$), ^{71}As (2α), ^{70}As ($2\alpha n$), ^{69}As($2\alpha 2n$), ^{69}Ge ($2\alpha pn$), ^{67}Ge ($2\alpha p3n$), ^{66}Ge ($2\alpha p4n$), ^{67}Ga (3α), ^{66}Ga ($3\alpha n$), ^{65}Ga ($3\alpha 2n$), and ^{61}Cu ($4\alpha 2n$) show significant enhancement over the PACE-2 predictions. This enhancement may be attributed to the fact that these residues have been populated not only by CF of ^{20}Ne with ^{59}Co, but also populated through the ICF process where, as the projectile breakup into α clusters (i.e., ^{20}Ne breakup into fragments ^{16}O + α and/or ^{12}C + ^{8}Be) and fusion of one of the clusters may take place with the target nucleus. It has also been shown that the sumrule model in its present form is unable to predict the cross sections of the residues produced in the ICF channel at about 5 MeV/nucleon energy. The analysis of the data also suggests that the projectile breakup probability leading to ICF increases with projectile energy. The comparison of the present data with similar data on ^{16}O+ ^{45}Sc [23,25] and ^{16}O + ^{74}Ge [24,25] systems suggests that ICF probability increases with mass-asymmetry of the interacting partners and supports the previous findings [8,10,19,26]. It is worth mentioning as a concluding remark that, at projectile energy below 8 MeV/nucleon, the incomplete fusion process plays an important role for the estimation of the total reaction cross section. Further, a large number of experimental data is needed for various projectile-target combinations. Measurement of recoil range distributions and spin distributions of the residues populated by complete fusion and incomplete fusion using the particle-gamma coincidence technique at the above projectile energies may provide a better understanding of the incomplete fusion process.

ACKNOWLEDGMENTS

The authors would like to express their grateful acknowledgment to the VECC, Kolkata, for providing the experimental facilities for carrying out the experiment. The authors are also thankful to Dr. S. K. Basu, Dr. S. K. Saha, and the operational staff of Cyclotron VECC, Kolkata, for providing the necessary facilities and their good cooperation during the course of this experiment. Authors are very much thankful to Dr. R. Tripathi, Radio-chemistry Division, Bhabha Atomic Research Centre (BARC), Tombay, for fruitful discussions and suggestions. The authors are also thankful to the Department of Physics, AMU, Aligarh, India, for providing the necessary facilities for this work. Financial support provided by UGC-DAE-CSR, Kolkata, and University Grants Commission, New Delhi, in the form of research projects are also acknowledged gratefully.

[1] M. Cavinato *et al.*, in *Heavy Ion Fusion*, edited by A. M. Stefanini (World Scientific, Singapore, 1994).
[2] P. E. Hodgson, E. Gadioli, and E. Gadioli Erba, *Introductory Nuclear Physics* (Clarendon Press, Oxford, 1997), Chap. 23.
[3] B. S. Tomar, A. Goswami, A. V. R. Reddy, S. K. Das, P. P. Burte, S. B. Manohar, and S. Prakash, Z. Phys. A **343**, 223 (1992).
[4] M. K. Sharma, Unnati, B. K. Sharma, B. P. Singh, H. D. Bhardwaj, Rakesh Kumar, K. S. Golda, and R. Prasad, Phys. Rev. C **70**, 044606 (2004).
[5] H. C. Britt and A. R. Quinton, Phys. Rev. **124**, 877 (1964).
[6] J. Galin, B. Gatty, D. Guerean, C. Rousset, V. C. Schlothauer-Voos, and X. Tarrago, Phys. Rev. C **9**, 1126 (1974).
[7] T. Inamura, M. Ishihara, T. Fukuda, T. Shimoda, and H. Hiruta, Phys. Lett. B **68**, 51 (1977).
[8] H. Morgenstern, W. Bohne, W. Galster, K. Grabisch, and A. Kyanowski, Phys. Rev. Lett. **52**, 1104 (1984).
[9] M. F. Vineyard *et al.*, Phys. Rev. C **45**, 1784 (1992).
[10] S. Chakrabarty, B. S. Tomar, A. Goswami, G. K. Gubbi, S. B. Manohar, A. Sharma, B. B. Kumar, and S. Mukherjee, Nucl. Phys. A **678**, 355 (2000).
[11] J. Wilczynski, K. Siwek-Wilczynska, J. Van Driel, S. Gongrijp, D. C. J. M. Hageman, R. V. F. Janssens, J. Lukasiak, R. H. Siemssen, and S. Y. Van der Werf, Nucl. Phys. A **373**, 109 (1982).
[12] T. Udagawa and T. Tamura, Phys. Rev. Lett. **45**, 1311 (1980).
[13] J. P. Bondorf, J. N. De, G. Fai, A. O. T. Karvinen, B. Jakobsson, and J. Randrup, Nucl. Phys. A **333**, 285 (1980).
[14] M. I. Sobel, P. J. Seimens, J. P. Bondorf, and H. A. Bethe, Nucl. Phys. A **251**, 502 (1975).

[15] P. Vergani, E. Gadioli, E. Vaciago, E. Fabrici, E. Gadioli Erba, M. Galmarini, G. Ciavola, and C. Marchetta, Phys. Rev. C **48**, 1815 (1993).
[16] M. Crippa, E. Gadioli, P. Vergani, G. Ciavola, C. Marchetta, and M. Bonardi, Z. Phys. A **350**, 121 (1994).
[17] B. B. Kumar, S. Mukherjee, S. Chakrabarty, B. S. Tomar, A. Goswami, and S. B. Manohar, Phys. Rev. C **57**, 743 (1998).
[18] B. B. Kumar, A. Sharma, S. Mukherjee, S. Chakrabarty, P. K. Pujari, B. S. Tomar, A. Goswami, S. B. Manohar, and S. K. Datta, Phys. Rev. C **59**, 2923 (1999).
[19] Pushpendra P. Singh, B. P. Singh, M. K. Sharma, Unnati, D. P. Singh, R. Prasad, R. Kumar, and K. S. Golda, Phys. Rev. C **77**, 014607 (2008).
[20] M. K. Sharma, Unnati, B. K. Sharma, B. P. Singh, R. Kumar, K. S. Golda, H. D. Bhardwaj, and R. Prasad, Nucl. Phys. A **776**, 83 (2006); M. K. Sharma, Unnati, B. K. Sharma, B. P. Singh, H. D. Bhardwaj, R. Kumar, K. S. Golda, and R. Prasad, Phys. Rev. C **70**, 044606 (2004).
[21] M. Dasgupta, P. R. S. Gomes, D. J. Hinde, S. B. Moraes, R. M. Anjos, A. C. Berriman, R. D. Butt, N. Carlin, J. Lubian, C. R. Morton, J. O. Newton, and A. Szanto de Toledo, Phys. Rev. C **70**, 024606 (2004).
[22] D. Singh, R. Ali, M. A. Ansari, M. H. Rashid, R. Guin, and S. K. Das, Phys. Rev. C **79**, 054601 (2009).
[23] D. Singh, M. Afzal Ansari, R. Ali, N. P. M. Sathik, and M. Ismail, J. Phys. Soc. Jpn. **75**, 104201 (2006).
[24] D. Singh, M. Afzal Ansari, R. Ali, N. P. M. Sathik, and M. Ismail, Chin. J. Phys. **46**, 27 (2008).
[25] D. Singh, Ph.D. thesis, Aligarh Muslim University, Aligarh, India (unpublished, 2008).
[26] R. Ali, D. Singh, M. Afzal Ansari, M. H. Rashid, R. Guin, and S. K. Das, J. Phys. G: Nucl. Part. Phys. **37**, 115101 (2010).
[27] A. Gavron, Phys. Rev. C **21**, 230 (1980).
[28] J. F. Ziegler, SRIM-2006, The Stopping Power and Range of Ions in Matter, 2006.
[29] MAESTRO, Data acquisition and analysis software coupled with EG & G *ORTEC* hardware.
[30] FREEDOM, Data acquisition and analysis software, designed to support the accelerator based experiments at the Inter-University Accelerator Centre (IUAC), New Delhi, India.
[31] *Table of Isotopes* , 8th ed., edited by R. B. Firestone and V. S. Shirley (Wiley, New York, 1996).
[32] M. Afzal Ansari, R. K. Y. Singh, M. L. Sehgal, V. K. Mittal, D. K. Avasthi, and I. M. Govil: Ann. Nucl. Energy **11**, 173 (1984).
[33] M. Cavinato, E. Fabrici, E. Gadioli, E. Gadioli Erba, P. Vergani, M. Crippa, G. Colombo, I. Redaelli, and M. Ripamonti, Phys. Rev. C **52**, 2577 (1995).
[34] R. Bass, Nucl. Phys. A **231**, 45 (1985).
[35] F. D. Becchetti and G. W. Greenlees, Phys. Rev. **182**, 1190 (1969).
[36] P. M. Endt, At. Data. Nucl. Data Tables **26**, 47 (1981).
[37] R. D. Evans, *Atomic Nucleus* (Mc Graw Hill, New York, 1955).
[38] K. S. Babu, R. Tripathi, K. Sudarshan, B. D. Shrivastava, A. Goswami, and B. S. Tomar, J. Phys. G: Nucl. Part. Phys. **29**, 1011 (2003).